energies

IMPACT FACTOR 3.9

CITESCORE 8.3

Article

Thermal Sprayed Oxide Coatings for Stainless Steel Containers Used with Molten Al–Si and Al–Cu–Si Phase Change Materials: Compatibility and Thermal Cycling Stability

Carolina Villada, Nuria Navarrete, Christian Semmler, Matthias Blum, Matthias Kolbe, Veronika Stahl, Werner Kraft and Florian Kargl

MDPI

https://doi.org/10.3390/en19204756

energies

MDPI

Article

Thermal Sprayed Oxide Coatings for Stainless Steel Containers Used with Molten Al–Si and Al–Cu–Si Phase Change Materials: Compatibility and Thermal Cycling Stability

Carolina Villada [1,*], Nuria Navarrete [1], Christian Semmler [2], Matthias Blum [2], Matthias Kolbe [1], Veronika Stahl [3], Werner Kraft [3] and Florian Kargl [1]

[1] Institut für Frontier Materials auf der Erde und im Weltraum, Abteilung für Metallische Werkstoffe und Prozesse (MWP), Deutsches Zentrum für Luft- und Raumfahrt (DLR), 51170 Köln, Germany; nuria.navarreteargiles@dlr.de (N.N.); matthias.kolbe@dlr.de (M.K.); florian.kargl@dlr.de (F.K.)

[2] Institut für Fertigungstechnologie Keramischer Bauteile (IFKB), Universität Stuttgart, 70569 Stuttgart, Germany; christian.semmler@ikmt.uni-stuttgart.de (C.S.)

[3] Institut für Fahrzeugkonzepte, Deutsches Zentrum für Luft- und Raumfahrt (DLR), 70569 Stuttgart, Germany; veronika.stahl@dlr.de (V.S.); werner.kraft@dlr.de (W.K.)

* Correspondence: carolina.villadavargas@dlr.de

Abstract

The application of aluminium-based metallic phase change materials (mPCMs) in latent heat thermal energy storage is limited by the poor compatibility of molten alloys with conventional stainless steel containers. This work evaluates thermally sprayed oxide coatings deposited directly on 304 stainless steel as protective barriers for molten Al–Si and Al–Cu–Si phase change materials. Alumina (Al_2O_3), zirconia (ZrO_2) and Al_2O_3/ZrO_2 (60/40 wt. %) coatings were produced by atmospheric plasma spraying (APS) and high-velocity suspension flame spraying (HVSFS) and assessed through coating characterisation, long-term static compatibility tests, thermal cycling experiments and thermal contact resistance measurements. APS coatings exhibited a pronounced dependence of coating thickness on spray angle, whereas the HVSFS coating provided a more uniform thickness distribution. After two weeks of static exposure, no reaction layer formation, coating dissolution or detectable elemental interdiffusion was observed for the investigated coating systems. For the Al_2O_3/Al–12.3 wt. % Si system, no coating degradation or interfacial reaction was detected after approximately 300 thermal cycles. Furthermore, average liquid thermal contact resistances of 0.31×10^{-3} and 0.39×10^{-3} m^2 K W^{-1} were measured for smooth and rough Al–Si/coating interfaces, respectively. These results demonstrate that thermally sprayed oxide coatings can effectively protect stainless steel from molten aluminium-based PCMs while providing design-relevant data for the development of high-temperature latent heat thermal energy storage systems.

Keywords: thermal energy storage; metallic phase change materials; ceramic coatings; thermal contact resistance

Check for updates

Academic Editor: Zacharie Tamainot-Telto

Received: 25 August 2026
Revised: 1 October 2026
Accepted: 6 October 2026
Published: 9 October 2026

Copyright: © 2026 by the authors. Licensee MDPI, Basel, Switzerland. This article is an open access article distributed under the terms and conditions of the Creative Commons Attribution (CC BY) license.

1. Introduction

Thermal energy storage (TES) systems serve to overcome the mismatch between energy generation and energy consumption demands by storing heat to be used later. TES technologies are applied in concentrating solar power (CSP), district heating and cooling, thermal management of residential buildings and electric vehicles [1–4]. In the transport sector, battery electric vehicles (BEVs) are expected to play a key role in reducing greenhouse

gas emissions. According to the International Energy Agency (IEA), road transport accounts for approximately 16% of global CO_2 emissions, making electrification an essential strategy for decarbonisation [5]. For battery electric buses (BEBs), limited driving range remains a major obstacle to large-scale deployment. TES-based thermal management offers the potential to extend driving range while improving battery performance and reliability by decoupling heat generation from electric motor demand [6,7].

Among the different TES concepts, latent heat storage based on metallic phase change materials (mPCMs) has attracted growing interest because of its high volumetric energy density, excellent thermal conductivity, and rapid charging and discharging capability compared with conventional salt- or organic-based PCMs [8–12]. Near-eutectic aluminium-based alloys, particularly Al–Si alloys, are considered promising candidates for high-temperature TES owing to their high latent heat, low material cost, and commercial availability [13]. Prototype-scale demonstrations have confirmed the potential of Al–Si alloys for thermal management in electric vehicles and concentrating solar power applications [14–16].

Despite these advantages, the widespread implementation of metallic PCMs is still limited by the lack of suitable container materials. During operation, molten aluminium alloys readily react with conventional steels through dissolution of alloying elements, interdiffusion and intermetallic formation, ultimately compromising the structural integrity of the storage container [17–19]. Therefore, the development of reliable barrier systems capable of simultaneously providing chemical stability, thermomechanical integrity and efficient heat transfer remains one of the major challenges for high-temperature latent heat storage.

Several ceramic coatings have been proposed as corrosion barriers for metallic PCMs in high-temperature TES applications [20,21]. Dindi et al. showed boron-nitride-coated stainless steel in contact with an Al–Si alloy to be stable for up to 720 melting and solidification cycles [22]. Thermally sprayed Ti(Al,O)/Al_2O_3 coating in contact with liquid Al showed no signs of reaction [23]. Plasma-sprayed coatings in contact with liquid Cu–Mg–Si at 820 °C performed well for Al_2O_3 as a coating and failed with Y_2O_3–stabilised ZrO_2 (YSZ) [24]. For P91 steel with Al_2O_3 and YSZ coatings in contact with Al–Si during 120 h at 900 °C, YSZ was found to be more stable due to its transformation toughening property [25]. Although some authors have demonstrated the corrosion resistance of ceramics against molten aluminium alloys, their use as container materials remains challenging due to the mismatch in thermal expansion coefficients between the different components of the system. Aluminium alloys (~23.6 × 10^{-6} °C^{-1}) and alloyed steel (~18 × 10^{-6} °C^{-1}) exhibit significantly higher thermal expansion compared to typical ceramics such as Al_2O_3 (~7.2 × 10^{-6} °C^{-1}) and ZrO_2 (~10.5 × 10^{-6} °C^{-1}). This difference leads to thermomechanical stresses during thermal cycling and ultimately leads to failure of both the coating and the container material [22,26]. Despite these limitations, ceramic coatings deposited directly onto steel substrates remain an attractive and practical solution. Their performance, however, strongly depends on factors such as coating microstructure, density, thickness, and adhesion, which govern their ability to withstand thermomechanical stresses and prevent interaction with molten aluminium alloys. Among oxide ceramics, Al_2O_3 and ZrO_2 are attractive candidates because of their high-temperature stability, chemical inertness toward molten aluminium alloys and widespread use in thermal spray applications.

Thermal spraying is a well-established technology for producing protective coatings by propelling molten or semi-molten particles onto a substrate, where they rapidly solidify. Among the available processes, atmospheric plasma spraying (APS) is widely used to produce dense ceramic coatings with good adhesion and low porosity [27]. High-velocity oxygen fuel (HVOF) spraying employs a high-pressure combustion process to generate

dense coatings with excellent adhesion [27]. High-velocity suspension flame spraying (HVSFS), an extension of the HVOF process using suspension feedstocks, enables the deposition of thinner and denser ceramic coatings with refined microstructures [28–31].

Although previous studies have demonstrated the chemical resistance of individual ceramic coatings against molten aluminium alloys, several important questions remain unresolved. Most investigations have focused on a single coating material or a single performance aspect, while systematic comparisons between different thermal spray technologies, coating architectures and aluminium-based PCMs remain scarce. Furthermore, the combined assessment of chemical compatibility, thermomechanical stability under representative thermal cycling conditions and thermal contact resistance has received little attention, despite its direct relevance for the engineering design of practical TES systems.

In this work, the stability and performance of thermally sprayed ceramic coatings on 304 stainless steel are systematically evaluated under conditions relevant to thermal energy storage. Three oxide coating systems produced by two thermal spray technologies are investigated. The coatings are assessed for their ability to prevent chemical interaction with molten aluminium-based alloys, specifically Al–12.3 wt. % Si and Al–23.54 wt. % Cu–9 wt. % Si. Long-term static corrosion experiments are conducted for up to two weeks at temperatures above the liquidus of the mPCMs. In addition, thermal cycling tests are performed to evaluate the resistance of the coating-substrate system to thermomechanical stresses under repeated melting-solidification cycles. Beyond chemical compatibility, the thermal performance of the mPCM-container interface is investigated. In particular, the thermal contact resistance at the solid–solid and solid-liquid interface between Al–12.3 wt. % Si and the coated steel substrate is analysed using laser flash analysis (LFA). The results presented herein contribute to a better understanding of the interactions between aluminium-based metallic PCMs and thermally sprayed ceramic coatings, providing design-relevant insights for the development of reliable container systems for high-temperature latent heat thermal energy storage.

2. Materials and Methods

2.1. Materials

The near-eutectic aluminium-silicon alloy was purchased from Oetinger Aluminium NU GmbH, Neu-Ulm, Germany. It had a measured composition of 87.33 Al, 12.30 Si and 0.37 (wt. %) other impurities such as 0.23 Fe, 0.06 Ti, 0.02 Mg, and 0.01 Mn (wt. %). The near-eutectic aluminium-copper-silicon alloy was purchased from IME Metallurgical Process Engineering and Metal Recycling at RWTH Aachen University, Aachen, Germany and had a measured composition of Al–23.54 wt. % Cu–9 wt. % Si and 0.59 (wt. %) other impurities (the majority of which was Zn). Type 304 is the most versatile and widely used stainless steel with 18 wt. % chromium and 8 wt. % nickel in its nominal composition. In this work, dish-shaped crucibles of 304 stainless steel (Hans-Erich Gemmel & Co. GmbH, Berlin, Germany) were manufactured and machined in-house with a minimum wall thickness of 2.5 mm, an outer diameter of 16 mm and an outer height of 6 mm. Figure 1 shows a representative photograph of the coated crucible and Al–12.3 wt. % Si mPCM before the reaction test. The powder material parameters used for the fabrication of the coatings are listed in Table 1.

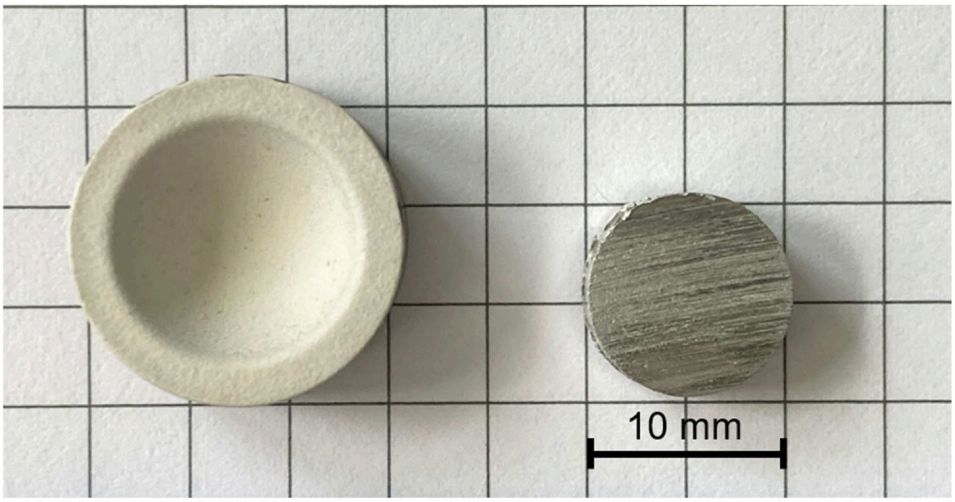


Figure 1. Al_2O_3-coated crucible (**left**) with Al–12.3 wt. % Si specimen (**right**) before the compatibility test.

Table 1. Powder material parameters used for the fabrication of the coatings.

Parameters	Al_2O_3	ZrO_2	Al_2O_3/ZrO_2
Technique	APS	APS	HVSFS
Powder material	Al_2O_3 99.7	ZrO_2 (monoclinic)	Al_2O_3/ZrO_2 60/40 wt. %
Powder size distribution	−20 + 5 µm	−40 + 10 µm	−4.5 + 1 µm custom
Powder supplier	Ceram	Amperit	Ceram

2.2. Thermal Sprayed Coatings

Surface preparation was done by sandblasting using α-Al_2O_3 F60 to achieve a rough surface where the molten ceramic particles can mechanically anchor. The Al_2O_3 and ZrO_2 coatings were manufactured by APS using a F6 torch by GTV Verschleißschutz GmbH (Luckenbach, Germany), while the Al_2O_3/ZrO_2 (60/40 wt. %) coating was produced by HVSFS using a TopGun torch also by GTV Verschleißschutz GmbH (Luckenbach, Germany). A detailed description of the spray setup can be found in a previous work [29]. The parameters for the coating application are shown in Table 2. Microhardness HV0.1 was measured using a Fischerscope system according to standard DIN EN ISO 14577 [32] with a Vickers test head and a force of 0.9807 N. Indentations were distributed over representative coating regions. At least 17 measurements were performed on each sample.

Table 2. Coating parameters of specimens produced by APS and HVSFS.

Parameters	Unit	Al_2O_3	ZrO_2	Parameters	Unit	Al_2O_3/ZrO_2
Torch	–	F6	F6	Torch	–	TopGun
Spray distance	mm	120	120	Nozzle	–	22-8-135
Current	A	500	500	Spray distance	mm	120
Argon	SLPM	40	40	Ethene	SLPM	60
Hydrogen	SLPM	8	8	Oxygen	SLPM	200
Relative speed part	min^{-1}	1000	1000	Relative speed part	mm s^{-1}	800
Robot trajectory	–	meander	Geometry adjusted	Robot trajectory	–	Meander
Powder supply	SLPM	5.0	5.0	Suspension feed rate	g min^{-1}	46
Powder feeder disc	mm	16	16	Powder content	wt. %	20
Powder feeder rotation	min^{-1}	6.0	5.0	Dispersant	–	Water + thixotropic agent

SLPM: standard litres per minute.

2.3. Static Reaction Test, Thermal Cycling and Microstructure Characterisation Techniques

Static experiments were conducted for 336 h to evaluate the operational compatibility of Al–12.3 wt. % Si and Al–23.54 wt. % Cu–9 wt. % Si alloys. Here, cylindrical pellets of approximately 800 mg were placed inside different crucibles of 304 stainless steel coated

with Al_2O_3, ZrO_2 and Al_2O_3/ZrO_2 (60/40 wt. %). The samples were held at 650 °C for Al–12.3 wt. % Si (melting temperature ~577 °C) and at 600 °C for Al–23.54 wt. % Cu–9 wt. % Si (melting temperature ~522 °C). To remove any volatile compounds, the coated crucibles had previously undergone an 8 h heat treatment under Argon at 600 °C prior to the experiment. The reaction furnace was vacuumed to 1×10^{-5} mbar and then backfilled with approximately 350 mbar of Argon 5.3 (99.993 mol. % purity). One independent specimen was used for each coating/alloy combination investigated in the static compatibility experiments.

Thermal cycling experiments were designed to reproduce representative operating conditions for latent heat thermal energy storage systems. The Al–12.3 wt. % Si alloy was selected as the candidate PCM for subsequent prototype development to ensure the practical relevance of the test conditions. The Al_2O_3 coating was selected for the thermal cycling experiments based on its demonstrated chemical compatibility with molten Al–12.3 wt. % Si during the static exposure tests and its relevance to the coating architecture considered for the intended application. It also represents the simplest coating architecture investigated in the present study. The thermal cycling program was established based on a representative operating scenario.

After an initial heating from room temperature to 610 °C, repeated melting–solidification cycles were performed between 520 and 610 °C. Each cycle consisted of holding the alloy at 610 °C for 10 min, cooling to 520 °C at a programmed rate of 18 °C min^{-1}, holding at 520 °C for 10 min, and reheating to 610 °C at a programmed rate of 18 °C min^{-1}. Each cycle had a duration of 30 min, resulting in approximately 30 thermal cycles during each 16 h driving period. Each daily operating sequence comprised a 16 h driving mode followed by an 8 h parking mode, during which the alloy was maintained at 610 °C in the fully molten state. The daily sequence was repeated until a cumulative molten-state exposure time of 160 h was reached, resulting in approximately 300 thermal cycles. The cumulative molten-state exposure was selected to enable comparison with the static compatibility experiments. One independent specimen was used for the thermal cycling experiment. Figure 2 shows the measured temperature–time (T–t) profile applied to the Al–12.3 wt. % Si alloy during the thermal cycling experiment.

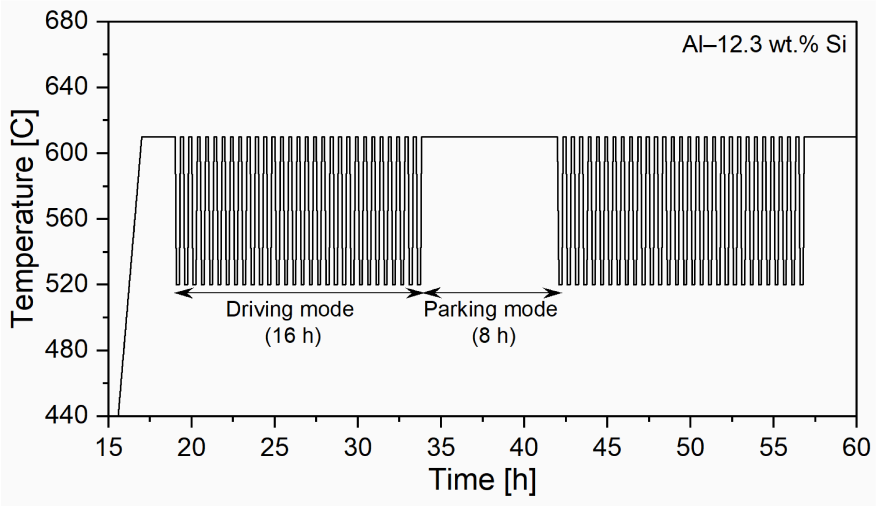


Figure 2. Programmed temperature–time (T–t) profile for the thermal cycling experiment with Al–12.3 wt. % Si. The cycling segment is shown as a magnified view of the repeated melting–solidification cycles.

Following the static reaction and thermal cycling experiments, the crucible and sample pairs were examined in terms of mass change and macroscopic appearance. The samples

were mounted in conductive epoxy resin (PolyFast, Struers, Ballerup, Denmark), sectioned and subsequently ground and polished to obtain a suitable surface finish for microstructural characterisation. The coating/alloy interface, coating integrity and possible elemental interdiffusion were evaluated by Scanning Electron Microscopy (SEM), Energy-dispersive X-ray spectroscopy (EDX) and electron backscatter diffraction (EBSD).

Differential scanning calorimetry (DSC) measurements were performed to determine the latent heat of the samples after the respective experiments. Samples weighing 20–30 mg were placed in platinum crucibles with alumina liners and platinum lids. Two heating and cooling runs were performed at a rate of 10 K min^{-1} using a NETZSCH DSC 404 C Pegasus® (NETZSCH-Gerätebau GmbH, Selb, Germany) coupled with a high-temperature furnace. Argon 5.3 was used as the purge gas at a volumetric flow rate of 50 mL min^{-1}. The latent heat was determined by integration of the melting peak from the second heating run using the NETZSCH Proteus® software, version 6.1.0.

2.4. Thermal Contact Resistance Measurements

Thermal contact resistance, r_c, expressed in m^2 K W^{-1}, represents the temperature drop across an interface per unit heat flux and is defined as

$$r_c = \Delta T / \dot{q}, \quad (1)$$

where ΔT is the temperature difference across the interface, expressed in K, and $\dot{q}$ is the heat flux, expressed in W m^{-2}.

The contact resistance between a 2 mm thick steel substrate and the deposited Al_2O_3 coating (Figure 3a,b) was measured over a temperature range from 100 °C to 650 °C. In addition, the contact resistance between the Al_2O_3-coated steel and the selected mPCM candidate Al–12.3 wt. % Si alloy was determined under the same conditions. The Al_2O_3 coatings used for the thermal contact resistance measurements were produced by APS by ICV Industrie Coating Verfahrenstechnik GmbH (Oberndorf am Neckar, Germany).

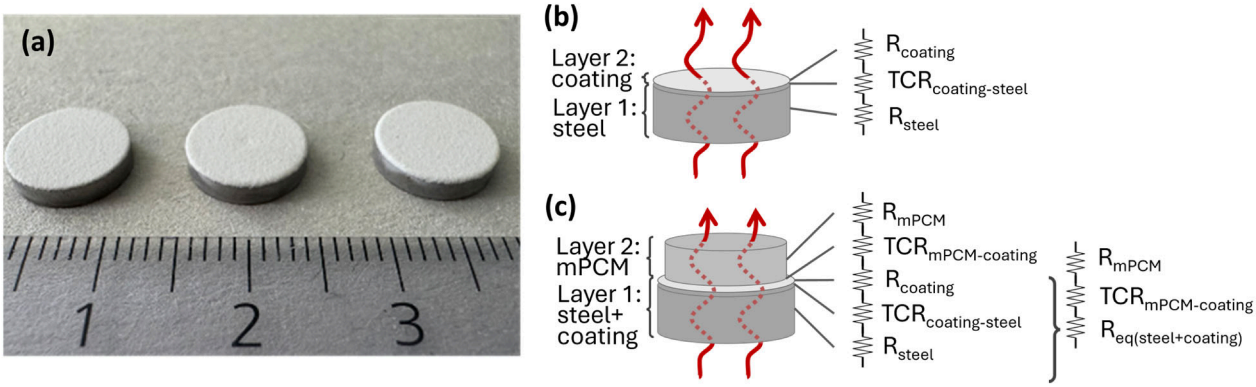


Figure 3. Samples for thermal contact resistance measurements with the LFA: (**a**) Al_2O_3-coated steel discs before experiments and layer configurations of (**b**) steel + Al_2O_3 coating and (**c**) steel + Al_2O_3 coating + Al–12.3 wt. % Si.

To measure thermal contact resistance, a light flash apparatus Netzsch LFA 467 HT Hyperflash® (NETZSCH-Gerätebau GmbH, Selb, Germany) was used. First, thermal diffusivities of 304 steel, 304 steel with Al_2O_3 coating and Al-12.3% Si alloy were measured using a standard model considering heat losses on the sides. Additionally, the specific heat of the 304 steel, alumina and Al-12.3% Si alloy was also measured in a range of 100–700 °C using a differential scanning calorimeter (NETZSCH DSC 404 C Pegasus®). Both parameters—thermal diffusivity and specific heat—along with density at room temperature, thermal expansion

coefficient and thickness of each layer are required as inputs to define the materials in the double-layer model used for contact resistance measurements. Once these parameters are defined, an analogy of the heat transfer through the different layers to an electric resistance circuit can be made. This includes the intrinsic thermal resistance of the material, related to the thermal conductivity and the thickness of each material, and the thermal contact resistance between the different layers. For simplicity in data analysis, the coated steel disk was treated as a single layer in the experiments involving Al–12.3 wt. % Si. A visual scheme of the models used and their analogy to an electric resistance is presented in Figure 3c.

In the thermal contact resistance measurements, the bottom part of the steel substrate and the top part of the mPCM pellet were coated with a graphite spray to avoid losses due to light reflection, replicating the behaviour of a black body. There was no external force applied to the two layers besides gravity. The influence of surface roughness was investigated by preparing Al–12.3 wt. % Si disks (~2 mm thickness) with different surface finishes. A smooth surface was obtained using 2400 grit SiC abrasive paper, while a rough surface was produced using 800 grit sandpaper. All measurements were conducted under a continuous flow of inert gas (argon 5.0, 50 mL min^{-1}).

3. Results and Discussion

3.1. As-Deposited Coating Characteristics

Representative cross-sectional micrographs of the as-deposited coatings prior to exposure are presented in Figure 4.

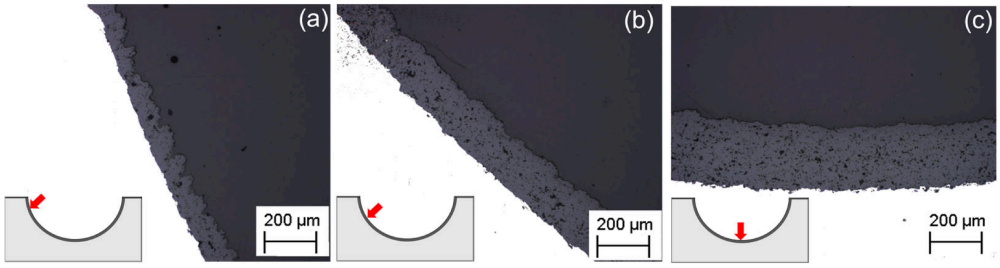


Figure 4. Optical micrographs of representative cross-sections of the APS Al_2O_3-coated crucible at (**a**) border, (**b**) 45° and (**c**) bottom zone.

For all coated crucibles, the hardness and coating thickness were measured prior to the experiments. The Al_2O_3 coating deposited by APS exhibited a strong dependence of thickness on the spray angle. At the bottom of the crucible, corresponding to a spray angle of 90°, a coating thickness of 254.3 ± 11.9 µm was obtained, whereas a significantly lower thickness of 82.9 ± 26.1 µm was measured in the flank region. This reduction in thickness at lower spray angles is attributed to decreased deposition efficiency, resulting in thinner coatings in the upper regions of the crucible [33–35].

The mismatch in thermal expansion between Al_2O_3 (~7.2 × 10^{-6} K^{-1}) and 304 stainless steel (~18 × 10^{-6} K^{-1}) is commonly considered a limiting factor for coating durability. Therefore, materials with thermal expansion coefficients closer to that of steel, such as ZrO_2 (~10.5 × 10^{-6} K^{-1}), are often proposed to improve thermomechanical compatibility. Similar to the Al_2O_3 coatings, the deposited ZrO_2 coatings exhibited a strong dependence of coating thickness on spray angle due to the crucible geometry. A maximum coating thickness of 266.6 ± 6.8 µm was measured at the bottom of the crucible, whereas a significantly lower thickness of 52.5 ± 8.0 µm was obtained in the flank region. In terms of hardness, the ZrO_2 coatings exhibited values approximately 58% lower than those of the alumina coatings.

Al_2O_3/ZrO_2 coatings were produced by high-velocity suspension flame spraying (HVSFS). In this case, a lower coating thickness was obtained, with a maximum value

of 67.8 ± 2.2 µm at the bottom of the crucible, resulting in a comparatively dense and uniform coating. In contrast to the APS coatings, the Al_2O_3/ZrO_2 coatings exhibited a more homogeneous thickness distribution across the crucible geometry, with reduced sensitivity to spray angle. The influence of spray angle on coating thickness for Al_2O_3-based systems has been previously reported by Müller et al. [36]. Concerning hardness, the Al_2O_3/ZrO_2 coatings exhibited lower values than pure Al_2O_3 coatings and were comparable to those of ZrO_2 coatings. A summary of the coating characteristics and representative optical micrographs of all thermally sprayed crucibles are presented in Table 3 and Figure 5, respectively.

Table 3. Thickness and hardness of the coatings at different measurement positions.

Thickness	Unit	Al_2O_3 Coated by APS	ZrO_2 Coated by APS	Al_2O_3/ZrO_2 Coated by HVSFS
Position 1: bottom	µm	254.3 ± 11.9	266.6 ± 6.8	67.8 ± 2.2
Position 2: 45°	µm	181.7 ± 14.4	147.5 ± 16.5	47.0 ± 0.9
Position 3: flank	µm	82.9 ± 26.1	52.5 ± 8.0	37.8 ± 3.6
Hardness HV0.1	–	1072.8 ± 62.4	627.7 ± 43.7	611.9 ± 104.0

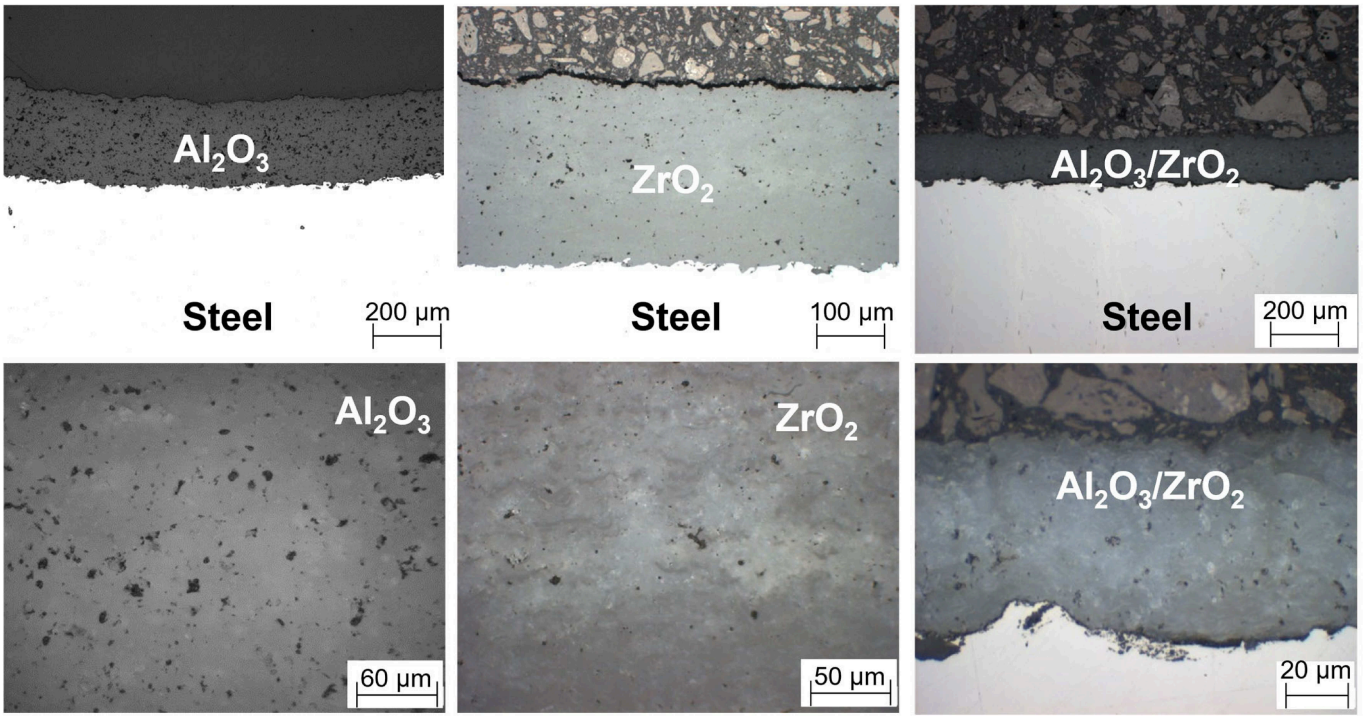


Figure 5. Morphology of cross-section at the bottom zone of APS-sprayed coatings before exposure in liquid aluminium alloys (**top**) and zoomed coating sections (**bottom**).

3.2. Chemical Compatibility with Molten Aluminium-Based PCMs

After two weeks of exposure at 650 °C, all coating systems exhibited excellent chemical compatibility with both Al–12.3 wt. % Si and Al–23.54 wt. % Cu–9 wt. % Si alloys. Independent of the coating material, SEM observations revealed no evidence of coating dissolution, interfacial reaction layers, or intermetallic phase formation at the coating/alloy interface. The individual material layers remained clearly distinguishable, indicating that the ceramic coatings effectively prevented direct interaction between the molten alloys and the 304 steel substrate. Furthermore, EDX analysis detected no enrichment of chromium or nickel from the stainless steel substrate within the alloy region, nor silicon enrichment within the substrate region. No detectable elemental interdiffusion was observed within the spatial resolution of the SEM/EDX analysis. In all cases, the characteristic microstructures

of both alloys were preserved after exposure. The Al–12.3 wt. % Si alloy exhibited a primary aluminium matrix with silicon-rich phases located in the interdendritic regions, whereas the Al–23.54 wt. % Cu–9 wt. % Si alloy retained its typical microstructure consisting of Al_2Cu dendrites together with aluminium dendrites and silicon precipitates.

The APS Al_2O_3 coating showed excellent structural integrity after exposure to both alloys. For the Al–12.3 wt. % Si system, the alloy pellet adhered to the crucible surface and formed a dark, crust-like oxide layer without measurable mass change. Although local variations in coating thickness were observed in the flank region, SEM examination revealed neither coating cracking nor degradation, even at higher magnifications. EDX analysis identified only trace amounts of iron and manganese exhibiting the characteristic Chinese-script morphology, which were already present in the as-received alloy. For the Al–23.54 wt. % Cu–9 wt. % Si system, partial coating detachment occurred locally during sample preparation, primarily in the flank region. However, no evidence of molten alloy infiltration or mechanical anchoring within the coating roughness was observed, and the coating remained structurally intact throughout the exposure.

The APS ZrO_2 coating exhibited a similar chemical behaviour to the Al_2O_3 coating. For the Al–12.3 wt. % Si alloy, the pellet also developed a dark, crust-like oxide layer, while the exposed ZrO_2 coating showed a darkened surface appearance. Although local coating thickness variations and edge detachment were observed during metallographic preparation, SEM analysis revealed no cracking or degradation of the ceramic layer. Likewise, the Al–23.54 wt. % Cu–9 wt. % Si system showed no signs of coating degradation or interfacial reaction. The alloy retained its characteristic Al_2Cu-rich microstructure, while the different material layers remained clearly distinguishable across the interface.

The HVSFS Al_2O_3/ZrO_2 coating exhibited slightly different mechanical behaviour while maintaining excellent chemical stability. For the Al–12.3 wt. % Si system, the sample surface showed a dull appearance together with a flaky oxide layer. In addition, localized cracks developed in the flank and 45° regions during sample preparation. Nevertheless, SEM observations revealed no evidence of coating dissolution or reaction products at the interface. Similar behaviour was observed after exposure to the Al–23.54 wt. % Cu–9 wt. % Si alloy, where localized cracks were also detected in the flank region. EBSD analysis identified an $Al_{70}Fe_{16}Si_6$-type phase in a few localized areas; however, the presence of iron was consistent with the initial alloy composition rather than interfacial degradation. As in the APS coatings, the alloy microstructure remained unchanged and no reaction layer developed.

Overall, despite minor differences in oxide morphology and the occurrence of localized coating detachment or cracking during specimen preparation, no evidence of chemical degradation of the ceramic coatings or interaction between the molten alloys and the 304 stainless steel substrate was detected in the investigated specimens after the two-week exposure. The results indicate that the three coating systems provide effective chemical barrier behaviour under the investigated static exposure conditions.

In contrast, bare 304 stainless steel cannot be directly used as a container material for molten Al alloys. As reported in the literature, molten aluminium readily attacks stainless steel through the dissolution of Ni and Cr, diffusion of liquid aluminium into the substrate, and the formation of brittle intermetallic phases [37]. Figure 6 summarizes the main microstructural observations obtained by SEM for all coating systems after static exposure. Representative SEM–EDX elemental mappings of the Al–12.3 wt. % Si | Al_2O_3 interface and Al–23.54 wt. % Cu–9 wt. % Si | Al_2O_3/ZrO_2 interface are shown in Figure 7 and Figure 8, respectively.

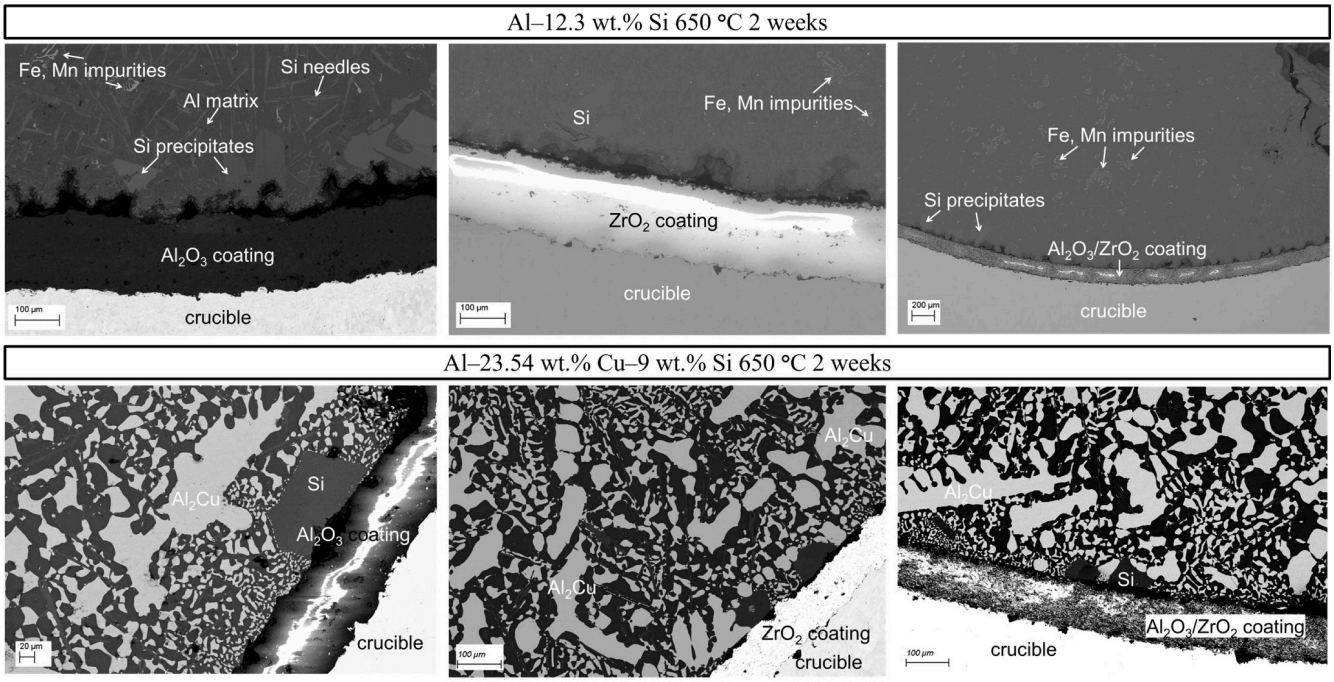


Figure 6. Cross-sectional SEM micrographs for all coating systems after static exposure.

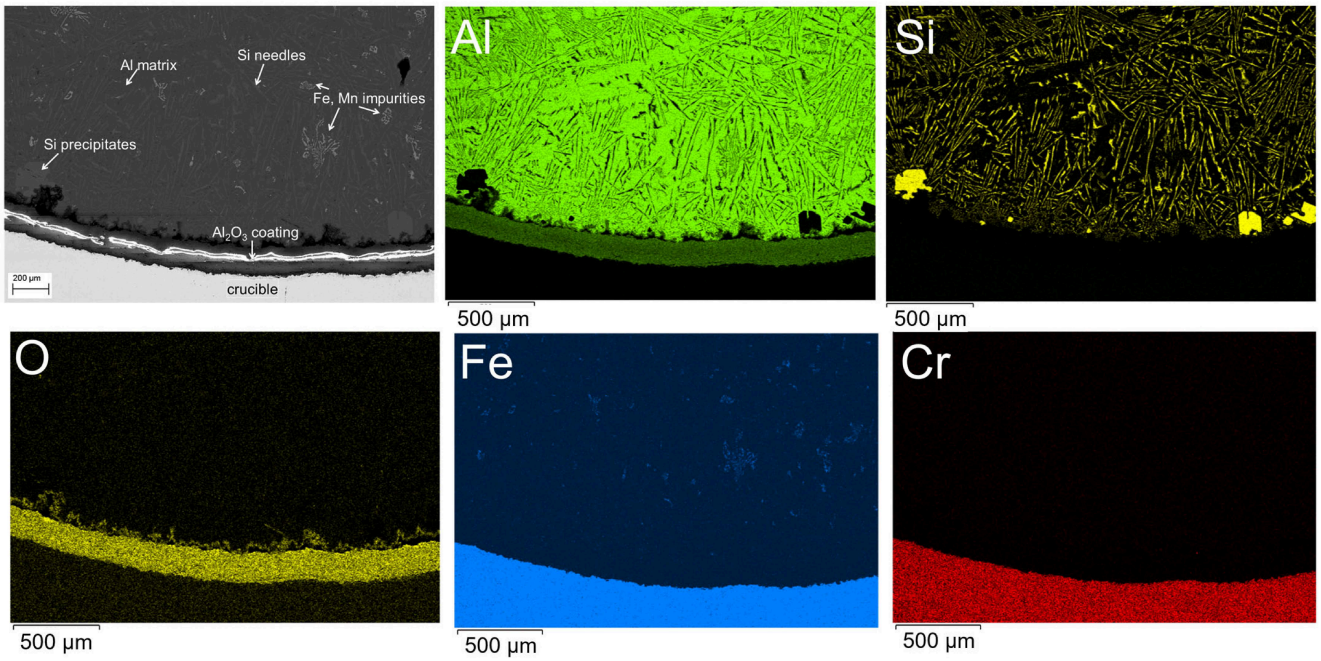


Figure 7. SEM–EDX elemental mapping of the Al–12.3 wt. % Si | Al_2O_3-coated specimen after static exposure at 650 °C for 336 h. The BSE image and corresponding elemental maps of Al, Si, O, Fe and Cr are shown from left to right. No detectable elemental interdiffusion across the alloy/coating/steel interfaces was observed within the spatial resolution of the SEM/EDX analysis.

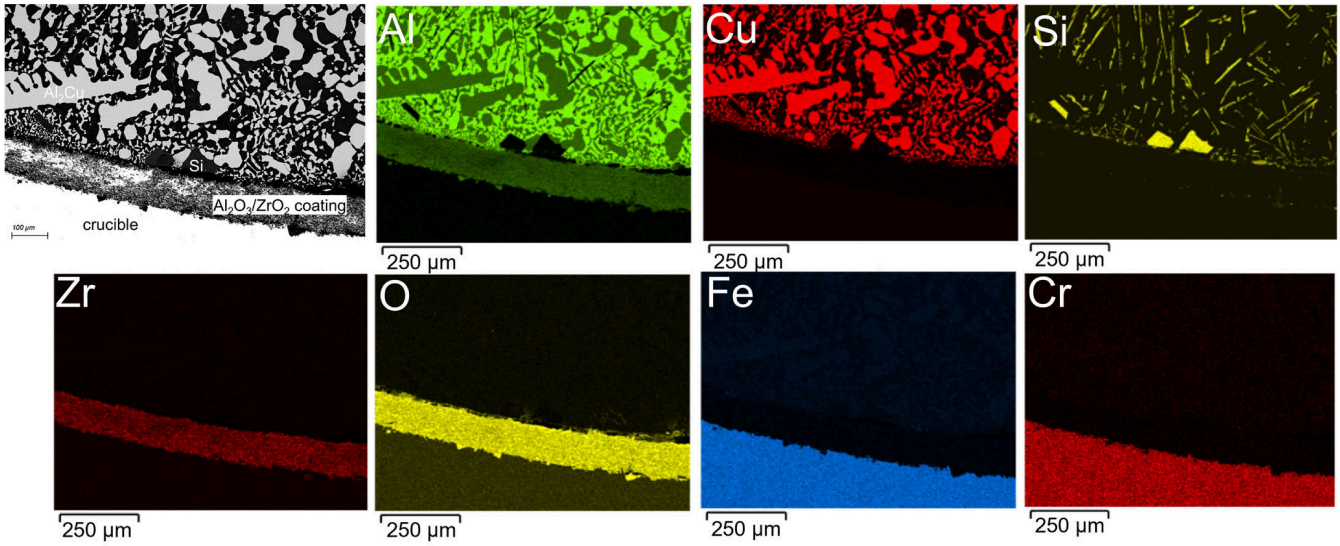


Figure 8. SEM–EDX elemental mapping of the Al–23.54 wt. % Cu–9 wt. % Si | Al_2O_3/ZrO_2-coated specimen after static exposure at 650 °C for 336 h. The BSE image and corresponding elemental maps of Al, Si, O, Fe and Cr are shown from left to right. No detectable elemental interdiffusion across the alloy/coating/steel interfaces was observed within the spatial resolution of the SEM/EDX analysis.

3.3. Thermal Cycling Stability of the Al–Si | SS304–Al_2O_3 System

While the static compatibility experiments demonstrated the chemical stability of the coating systems under isothermal conditions, practical latent heat thermal energy storage systems operate under repeated melting–solidification cycles. Therefore, thermal cycling experiments were performed to evaluate the thermomechanical stability of the selected coating system under representative operating conditions. The Al–12.3 wt. % Si alloy was selected as the candidate material due to its relevance for the intended application and its use in the prototype design. The Al_2O_3 coating was selected for the thermal cycling experiments because it demonstrated effective chemical compatibility with the molten Al–12.3 wt. % Si alloy during the static exposure tests, while representing the simplest and potentially more cost-effective coating architecture investigated. The selected thermal profile comprised approximately 300 melting–solidification cycles and a cumulative molten-state exposure time of 160 h, as previously described in Section 2.3.

Following thermal cycling, visual inspection revealed the formation of a continuous dark oxide layer covering the exposed surface of the Al–12.3 wt. % Si alloy. In contrast, no visible degradation of the Al_2O_3 coating was observed. Cross-sectional SEM observations confirmed that the Al_2O_3 coating maintained its structural integrity after thermal cycling. No coating dissolution, interfacial reaction layer or penetration of the molten alloy into the coating was detected. Likewise, EDX analysis revealed no detectable enrichment of Fe, Cr or Ni at the coating/alloy interface. No elemental interdiffusion was detected within the spatial resolution of the SEM/EDX analysis. No significant changes in the characteristic microstructure of the Al–12.3 wt. % Si alloy were observed after thermal cycling. These observations indicate that repeated melting and solidification did not compromise the chemical barrier function of the Al_2O_3 coating. This is confirmed by the cross-sectional SEM analysis shown in Figure 9.

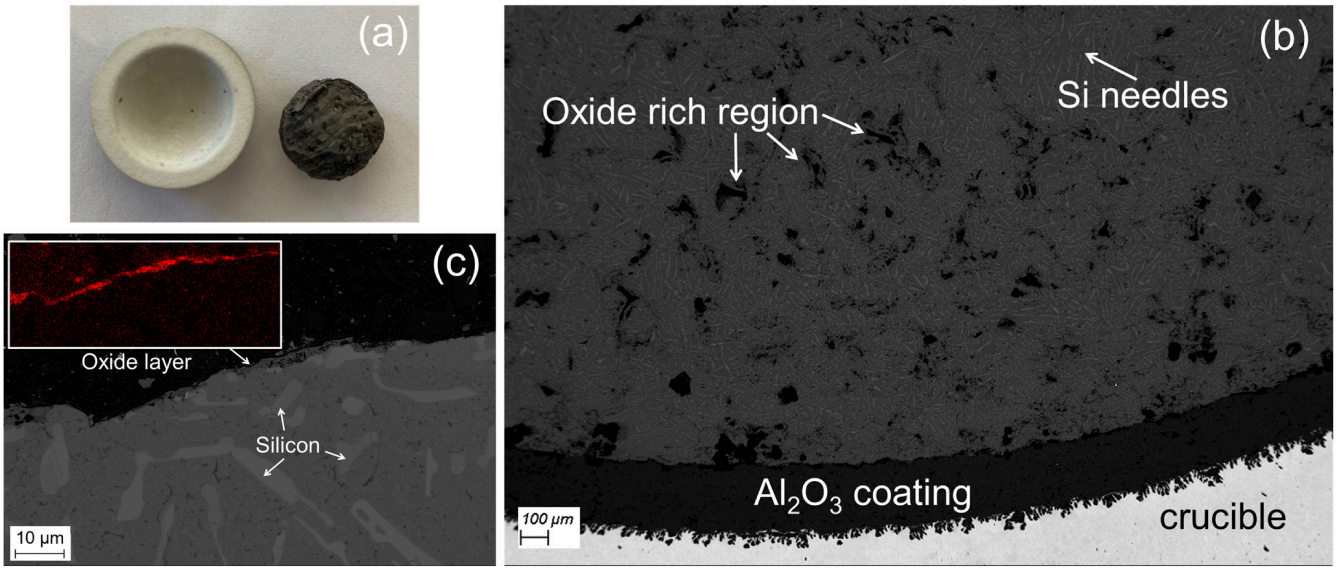


Figure 9. Thermal cycling behaviour of the Al–12.3 wt. % Si | SS304–Al_2O_3 system after approximately 300 melting–solidification cycles: (**a**) visual appearance of the cycled sample showing the surface oxide layer, (**b**) cross-sectional SEM micrograph of the coating/alloy interface and (**c**) Al–12.3 wt. % Si upper surface.

The effect of thermal cycling on the latent heat storage capacity of the Al–12.3 wt. % Si alloy was evaluated by DSC measurements performed on the fresh alloy and on samples collected after the static compatibility tests and thermal cycling. All measurements were conducted using the same instrument calibration to ensure comparability between the investigated conditions. The fresh Al–12.3 wt. % Si alloy exhibited a latent heat of 475.4 ± 6.1 J g^{-1}, while the sample subjected to approximately 300 melting–solidification cycles exhibited a latent heat of 465.9 ± 3.7 J g^{-1}. This corresponds to a decrease of approximately 2.0% relative to the fresh material, indicating that the latent heat storage capacity was essentially maintained after thermal cycling under the investigated conditions. The samples subjected to static compatibility tests exhibited latent heat values of 444.7 ± 9.0 J g^{-1} for Al_2O_3, 460.2 ± 6.2 J g^{-1} for ZrO_2, and 454.3 ± 1.8 J g^{-1} for Al_2O_3/ZrO_2. These values remained within a comparable range, with no clear systematic variation among the investigated coating systems. The DSC results obtained for the different coating systems are summarized in Figure 10.

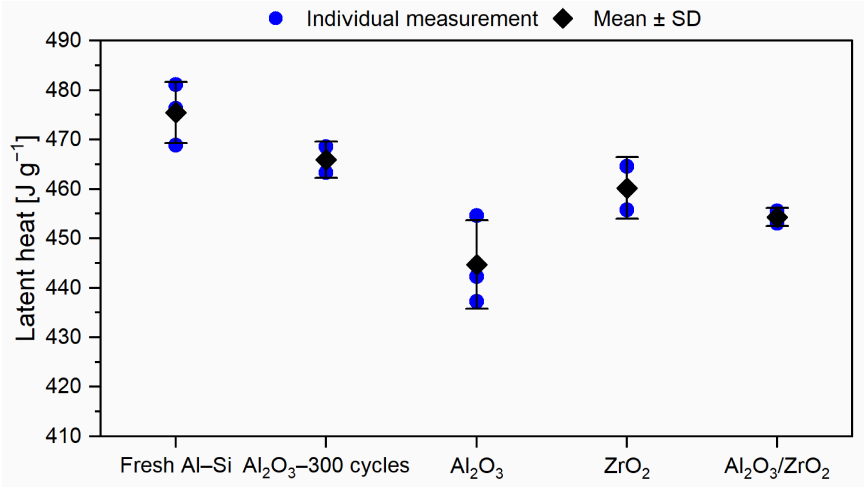


Figure 10. Latent heat of the Al–12.3 wt. % Si alloy before and after static exposure with different ceramic coatings and after approximately 300 thermal cycles. Circles represent individual measurements, diamonds indicate mean values, and error bars represent standard deviations.

3.4. Thermal Contact Resistance of the Al–Si | SS304–Al_2O_3 Interface

Besides chemical compatibility, the thermal performance of the container–PCM interface is a key parameter for latent heat thermal energy storage systems. Even when chemical degradation is prevented, a high thermal contact resistance can reduce charging and discharging rates by limiting heat transfer across the interface. Therefore, the thermal contact resistance at the Al–12.3 wt. % Si | SS304–Al_2O_3 interface was investigated over the relevant operating temperature range to assess the thermal performance of the coated container system.

The magnitude of thermal contact resistance depends on several factors, including surface roughness. The smooth and rough surface conditions considered in this study are representative of typical interfaces encountered in practical thermal storage systems. Despite its importance, the thermal contact resistance between Al_2O_3 coatings and metallic substrates has not been extensively studied, with most available data originating from thermal management applications. Reported values for steel–ceramic interfaces range from 0.1 to 0.4 $\times$ 10^{-3} m^2 K W^{-1} between room temperature and 400 °C [38].

Figure 11 presents the experimentally measured thermal contact resistance values, with standard deviations indicated as error bars. The corresponding linear regression results for the steel–Al_2O_3 interface, as well as for the Al–12.3 wt. % Si alloy in contact with smooth and rough surfaces, are summarized in Table 4. The average thermal contact resistance in the liquid state was determined to be 0.31 $\times$ 10^{-3} m^2 K W^{-1} for the smooth surface and 0.39 $\times$ 10^{-3} m^2 K W^{-1} for the rough surface.

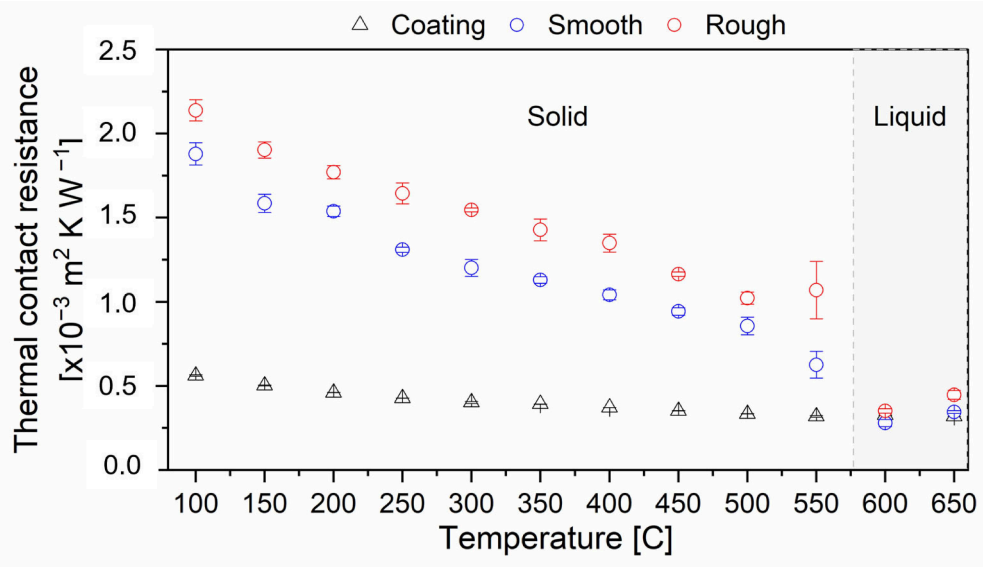


Figure 11. Experimental thermal contact resistance at the Al–12.3 wt. % Si | SS304–Al_2O_3 interface in solid and liquid phases.

Table 4. Linear regression results of thermal contact resistance at the Al–12.3 wt. % Si | SS304–Al_2O_3 interface for smooth and rough surface conditions.

Sample	Thermal Contact Resistance, r_c (m^2 K W^{-1})
SS304 + Al_2O_3 coating	$r_c = \begin{cases} -0.5 \times 10^{-6} + 0.57 \times 10^{-3}\,T & \text{if } T < 850K \\ 0.32 \times 10^{-3} & \text{if } T > 850K \end{cases}$
SS304 + Al_2O_3 coating + AlSi smooth	$r_c = \begin{cases} -2.4 \times 10^{-6} + 1.99 \times 10^{-3}\,T & \text{if } T < 850K \\ 0.31 \times 10^{-3} & \text{if } T > 850K \end{cases}$
SS304 + Al_2O_3 coating + AlSi rough	$r_c = \begin{cases} -2.4 \times 10^{-6} + 2.29 \times 10^{-3}\,T & \text{if } T < 850K \\ 0.39 \times 10^{-3} & \text{if } T > 850K \end{cases}$

T is the temperature, expressed in K.

The observed decrease in thermal contact resistance at elevated temperatures is likely associated with improved interfacial contact between the molten alloy and the ceramic coating. Under the investigated conditions, the smooth interface exhibited a lower average TCR than the rough interface. This observation highlights the dependence of interfacial heat transfer on the specific contact conditions and surface characteristics. Consequently, efficient heat transfer can be maintained under operating conditions relevant to latent heat thermal energy storage.

The compatibility, thermal cycling and thermal contact resistance experiments were performed using simplified crucible geometries to facilitate material characterisation and microstructural analysis. These geometries were not intended to represent the final container configuration. The coating system investigated in this work is intended for application on flat stainless steel plates representative of a laboratory-scale latent heat thermal energy storage system. Figure 12 illustrates the envisaged container geometry, providing the application context for the material selection and compatibility assessment presented in this study.

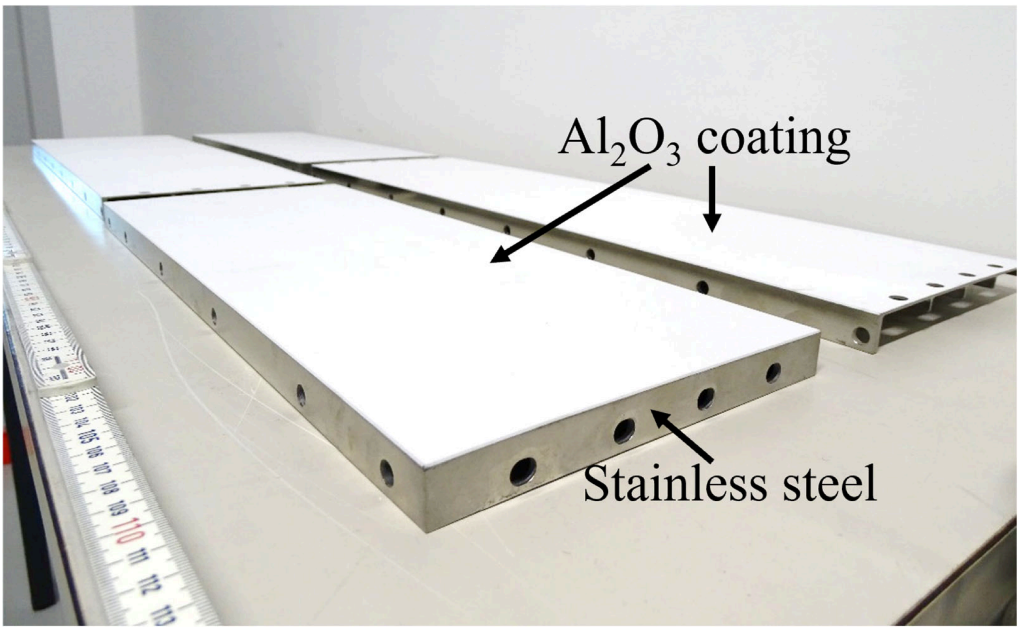


Figure 12. Planar Al_2O_3-coated stainless steel container plates representing the intended geometry for aluminium-based latent heat thermal energy storage systems (dimensions approx. 50 × 50 × 10 cm).

4. Conclusions

This work systematically evaluated the chemical compatibility, thermomechanical stability and thermal performance of thermally sprayed oxide coatings on 304 stainless steel intended for molten aluminium-based phase change materials. Three coating systems were investigated under static compatibility conditions, while thermal cycling was performed only for the Al_2O_3/Al–12.3 wt. % Si system. All investigated coating systems showed chemical stability in contact with molten Al–12.3 wt. % Si and Al–23.54 wt. % Cu–9 wt. % Si under the static exposure conditions, with no evidence of interfacial reaction or coating degradation. No detectable elemental interdiffusion was observed within the spatial resolution of the SEM/EDX analysis, supporting the chemical barrier function of the investigated coating systems.

Thermal cycling experiments showed that the Al_2O_3 coating remained chemically and mechanically stable after approximately 300 melting–solidification cycles. Additional DSC measurements indicated that the latent heat storage capacity of the Al–12.3 wt. % Si

alloy was essentially maintained after thermal cycling, with no substantial degradation of the bulk latent heat detected under the investigated conditions. No evidence of coating degradation or interfacial reaction was observed, indicating that the barrier function of the coating was preserved under the investigated operating conditions.

Experimental thermal contact resistance data obtained for the Al–12.3 wt. % Si | SS304–Al_2O_3 interface showed that interfacial heat transfer depends on the contact conditions and surface characteristics. The measured thermal contact resistance decreased with increasing temperature, indicating improved thermal contact after melting while remaining compatible with efficient heat transfer under relevant operating conditions.

The combined evaluation of chemical compatibility, thermal cycling stability and thermal contact resistance provides a comprehensive basis for selecting ceramic coating systems for aluminium-based latent heat thermal energy storage applications.

Further validation under application-relevant conditions will support the assessment of the coating systems' long-term performance and facilitate their potential implementation in thermal energy storage applications.

Author Contributions: Conceptualization, C.V. and C.S.; methodology, C.V., N.N., C.S. and M.B.; validation, C.V., N.N., C.S. and M.B.; formal analysis, C.V., N.N., M.K., C.S. and M.B.; investigation, C.V. and N.N.; data curation, C.V., N.N., M.K., C.S. and M.B.; writing—original draft preparation, C.V., C.S. and M.B.; writing—review and editing, C.V., N.N., V.S., W.K. and F.K.; supervision, F.K.; project administration, F.K.; funding acquisition, F.K. All authors have read and agreed to the published version of the manuscript.

Funding: This research was funded internally within the project Fokusanwendungen, Fahrzeugstruktur, Antriebsstrang, Energiemanagement (FFAE) and Long Haul Robot Truck (LHRT). This research received no external funding.

Data Availability Statement: The data presented in this study is available on request from the corresponding author.

Acknowledgments: The authors gratefully acknowledge Julie Boyadjian for performing DSC measurements.

Conflicts of Interest: The authors declare no conflicts of interest.

Abbreviations

The following abbreviations are used in this manuscript:

TES	Thermal energy storage
CSP	Concentrating solar power
mPCM	Metallic phase change material
APS	Atmospheric plasma spraying
HVOF	High-velocity oxygen fuel
HVSFS	High-velocity suspension flame spraying
DSC	Differential scanning calorimetry
LFA	Laser flash analysis
TCR	Thermal contact resistance
EBSD	Electron backscatter diffraction
EDX	Energy-dispersive X-ray spectroscopy
SEM	Scanning electron microscopy

References

1. Khare, S.; Dell'Amico, M.; Knight, C.; McGarry, S. Selection of materials for high temperature latent heat energy storage. *Sol. Energy Mater. Sol. Cells* **2012**, *107*, 20–27. [CrossRef]
2. Opolot, M.; Zhao, C.; Liu, M.; Mancin, S.; Bruno, F.; Hooman, K. A review of high temperature ($\geq$ 500 °C) latent heat thermal energy storage. *Renew. Sustain. Energy Rev.* **2022**, *160*, 112293. [CrossRef]
3. Nicolalde, J.F.; Cabrera, M.; Martínez-Gómez, J.; Salazar, R.B.; Reyes, E. Selection of a phase change material for energy storage by multi-criteria decision method regarding the thermal comfort in a vehicle. *J. Energy Storage* **2022**, *51*, 104437. [CrossRef]
4. Murphy, C.; Sun, Y.; Cole, W.; Maclaurin, G.; Turchi, C.; Mehos, M. *The Potential Role of Concentrating Solar Power Within the Context of DOE's 2030 Solar Cost Target*; National Renewable Energy Laboratory: Golden, CO, USA, 2019.
5. IEA. Global EV Outlook 2021. Available online: https://www.iea.org/reports/global-ev-outlook-2021 (accessed on 8 January 2026).
6. Rodrigues, A.L.P.; Seixas, S.R.C. Battery-electric buses and their implementation barriers: Analysis and prospects for sustainability. *Sustain. Energy Technol. Assess.* **2022**, *51*, 101896. [CrossRef]
7. Xie, P.; Jin, L.; Qiao, G.; Lin, C.; Barreneche, C.; Ding, Y. Thermal energy storage for electric vehicles at low temperatures: Concepts, systems, devices and materials. *Renew. Sustain. Energy Rev.* **2022**, *160*, 112263. [CrossRef]
8. Jankowski, N.R.; McCluskey, F.P. A review of phase change materials for vehicle component thermal buffering. *Appl. Energy* **2014**, *113*, 1525–1561. [CrossRef]
9. Fernández, A.I.; Camila, B.; Martin, B.; Mercè, S.; Frank, B.; Luisa, F.C. Considerations for the use of metal alloys as phase change materials for high temperature applications. *Sol. Energy Mater. Sol. Cells* **2017**, *171*, 275–281. [CrossRef]
10. Costa, S.C.; Kenisarin, M. A review of metallic materials for latent heat thermal energy storage: Thermophysical properties, applications, and challenges. *Renew. Sustain. Energy Rev.* **2022**, *154*, 111812. [CrossRef]
11. Sun, M.; Liu, T.; Sha, H.; Li, M.; Liu, T.; Wang, X.; Chen, G.; Wang, J.; Jiang, D. A review on thermal energy storage with eutectic phase change materials: Fundamentals and applications. *J. Energy Storage* **2023**, *68*, 107713. [CrossRef]
12. Mallya, N.; Suter, C.; Binder, S.; Barbato, M.; Ortona, A.; Haussener, S. Multi-configuration evaluation of a megajoule-scale high-temperature latent thermal energy storage test-bed. *Appl. Therm. Eng.* **2022**, *214*, 118697. [CrossRef]
13. Villada, C.; Navarrete, N.; Rawson, A.; Kolbe, M.; Stahl, V.; Kraft, W.; Kargl, F. Recycling of aluminium scrap into phase change materials for high-temperature storage applications: Thermophysical properties and microstructural characterisation. *J. Energy Storage* **2023**, *72*, 108822. [CrossRef]
14. Luo, C.; Xie, P.; Chen, G.; Mao, L.; Liu, L.; Jin, L.; Cheng, Z.; Xu, J.; Qiao, G. Prototype design and experimental study of a metal alloy-based thermal energy storage system for heat supply in electric vehicles. *J. Energy Storage* **2022**, *51*, 104393. [CrossRef]
15. Rea, J.E.; Oshman, C.J.; Singh, A.; Alleman, J.; Parilla, P.A.; Hardin, C.L.; Olsen, M.L.; Siegel, N.P.; Ginley, D.S.; Toberer, E.S. Experimental demonstration of a dispatchable latent heat storage system with aluminum-silicon as a phase change material. *Appl. Energy* **2018**, *230*, 1218–1229. [CrossRef]
16. Rea, J.E.; Oshman, C.J.; Singh, A.; Alleman, J.; Buchholz, G.; Parilla, P.A.; Adamczyk, J.M.; Fujishin, H.N.; Ortiz, B.R.; Braden, T.; et al. Prototype latent heat storage system with aluminum-silicon as a phase change material and a Stirling engine for electricity generation. *Energy Convers. Manag.* **2019**, *199*, 111992. [CrossRef]
17. Rawson, A.; Villada, C.; Kolbe, M.; Stahl, V.; Kargl, F. Suitability of aluminium copper silicon eutectic as a phase change material for thermal storage applications: Thermophysical properties and compatibility. *Energy Storage* **2021**, *4*, e299. [CrossRef]
18. Villada, C.; Rawson, A.; Navarrete, N.; Kolbe, M.; Kargl, F. Copper-magnesium eutectic as phase change material for thermal storage applications: Thermophysical properties and compatibility. *J. Energy Storage* **2022**, *52*, 105069. [CrossRef]
19. Stahl, V.; Shi, Y.; Kraft, W.; Lanz, T.; Vetter, P.; Jemmali, R.; Kessel, F.; Koch, D. C/C-SiC component for metallic phase change materials. *Int. J. Appl. Ceram. Technol.* **2020**, *17*, 2040–2050. [CrossRef]
20. Ryo, F.; Takahiro, N.; Chunyu, Z.; Nan, S.; Noriyuki, O.; Tomohiro, A. Macro-encapsulation of metallic phase change material using cylindrical-type ceramic containers for high-temperature thermal energy storage. *Appl. Energy* **2016**, *170*, 324–328. [CrossRef]
21. Ryo, F.; Takahiro, N.; Chunyu, Z.; Nan, S.; Noriyuki, O.; Tomohiro, A. Thermal analysis of Al–Si alloys as high-temperature phase-change material and their corrosion properties with ceramic materials. *Appl. Energy* **2016**, *163*, 1–8. [CrossRef]
22. Dindi, A.; Lopez Ferber, N.; Gloss, D.; Rilby, E.; Calvet, N. Compatibility of an Aluminium-Silicon metal alloy-based phase change material with coated stainless-steel containers. *J. Energy Storage* **2020**, *32*, 101961. [CrossRef]
23. Salman, A.; Gabbitas, B.L.; Cao, P.; Zhang, D.L. The performance of thermally sprayed titanium based composite coatings in molten aluminium. *Surf. Coat. Technol.* **2011**, *205*, 5000–5008. [CrossRef]
24. Withey, E.; Kruizenga, A.; Andraka, C.; Gibbs, P. Plasma sprayed coatings for containment of Cu-Mg-Si metallic phase change material. *Surf. Coat. Technol.* **2016**, *304*, 117–124. [CrossRef]
25. Tiwari, V.; Periaswamy, S. Compatibility of structural materials with AlSi12 alloys-based phase change material and increasing the corrosion resistance by ceramic coatings. *J. Energy Storage* **2023**, *72*, 108526. [CrossRef]
26. Yan, M.; Fan, Z. Review Durability of materials in molten aluminum alloys. *J. Mater. Sci.* **2001**, *36*, 285–295. [CrossRef]

27. Tejero-Martin, D.; Rezvani Rad, M.; McDonald, A.; Hussain, T. Beyond Traditional Coatings: A Review on Thermal-Sprayed Functional and Smart Coatings. *J. Therm. Spray Technol.* **2019**, *28*, 598–644. [CrossRef]
28. Killinger, A.; Kuhn, M.; Gadow, R. High-Velocity Suspension Flame Spraying (HVSFS), a new approach for spraying nanoparticles with hypersonic speed. *Surf. Coat. Technol.* **2006**, *201*, 1922–1929. [CrossRef]
29. Blum, M.; Gyoktepeliler-Akin, E.; Killinger, A. High velocity suspension flame spraying of AlN/Al_2O_3 composite coatings. *Surf. Coat. Technol.* **2022**, *441*, 128588. [CrossRef]
30. Michalak, M.; Latka, L.; Sokolowski, P.; Toma, F.-L.; Myalska, H.; Denoirjean, A.; Ageorges, H. Microstructural, mechanical and tribological properties of finely grained Al_2O_3 coatings obtained by SPS and S-HVOF methods. *Surf. Coat. Technol.* **2020**, *404*, 126463. [CrossRef]
31. Bai, M.; Maher, H.; Pala, Z.; Hussain, T. Microstructure and phase stability of suspension high velocity oxy-fuel sprayed yttria stabilised zirconia coatings from aqueous and ethanol based suspensions. *J. Eur. Ceram. Soc.* **2018**, *38*, 1878–1887. [CrossRef]
32. *DIN EN ISO 14577-1:2015-11*; Metallic Materials–Instrumented Indentation Test for Hardness and Materials Parameters—Part 1: Test Method. Beuth Verlag: Berlin, Germany, 2015.
33. Smith, M.F.; Neiser, R.A.; Dykhuizen, R.C. *An Investigation of the Effects of Droplet Impact Angle in Thermal Spray Deposition*; ASM International: Materials Park, OH, USA, 1994.
34. Li, C.-J.; Li, W.-Y.; Wang, Y.-Y.; Yang, G.-J.; Fukanuma, H. A theoretical model for prediction of deposition efficiency in cold spraying. *Thin Solid Films* **2005**, *489*, 79–85. [CrossRef]
35. Floristán, M.; Müller, P.; Gebhardt, A.; Killinger, A.; Gadow, R.; Cardella, A.; Li, C.; Stadler, R.; Zangl, G.; Hirsch, M.; et al. Development and testing of 140GHz absorber coatings for the water baffle of W7-X cryopumps. *Fusion Eng. Des.* **2011**, *86*, 1847–1850. [CrossRef]
36. Müller, P. *Prozessdiagnostik und Beschichtungstechnik beim Plasma- und Hochgeschwindigkeitsflammspritzen von Keramischen Suspensionen*; Shaker Verlag: Aachen, Germany, 2016.
37. Balloy, D.; Tissier, J.-C.; Giorgi, M.-L.; Briant, M. Corrosion Mechanisms of Steel and Cast Iron by Molten Aluminum. *Metall. Mater. Trans. A* **2010**, *41*, 2366–2376. [CrossRef]
38. Jussi Silvonen, E.L.; Mikko, U. The thermal contact resistance of a steel-ceramic interface with oxide intermediates. *Cogent Eng.* **2020**, *7*, 1720057. [CrossRef]

Disclaimer/Publisher's Note: The statements, opinions and data contained in all publications are solely those of the individual author(s) and contributor(s) and not of MDPI and/or the editor(s). MDPI and/or the editor(s) disclaim responsibility for any injury to people or property resulting from any ideas, methods, instructions or products referred to in the content.